

Synthesis and characterization of coaxial SnO₂-SiO_x core-shell nanorods

Hong Quan Liu¹ · Ting Yuan¹ · HongZhi Cui¹ · ZhiYing Chu¹ · YiJie Gu¹

Received: 21 March 2016 / Accepted: 23 May 2016 / Published online: 13 June 2016
© Springer-Verlag Berlin Heidelberg 2016

Abstract Free-standing coaxial SnO₂-SiO_x core-shell nanorods were synthesized in a kinetically controlled manner by the chemical vapor transport method. The free-standing SnO₂-SiO_x core-shell nanorods appear with uniform morphology exhibiting smooth surface, diameters of 100–200 nm, and length of 1 μm. The low oxygen partial pressure and high reaction temperature are advantageous to form the (101) surface, which decreases the (101) crystal surface energy. The [101] growth direction in our process also satisfies the lowest energy principle in thermodynamics due to change of (101) surface energy. A heterogeneous nucleation site was provided by the SiO_x dismutation reaction, and the formation of core-shell (SnO₂-SiO_x) structure should result from the phase separation energy. The free-standing coaxial SnO₂-SiO_x heterostructured nanorods grow by modification of the mass transfer coefficient. As-grown depositions show shrimp-like, flower-like, and worm-like morphologies under a higher mass transfer coefficient. Formation of the free-standing core-shell structure depends on the vertical growth mechanism.

1 Introduction

SnO₂ is a promising key functional material for a wide range of practical applications. It is widely used as a gas sensor, an electrode material for energy conversion and

storage applications, and has an application in field emission and photoluminescence [1–4]. SnO₂ nanocrystals, hollow spheres, nanowires, nanobelts, and nanotubes have been synthesized by hydrothermal, inverse microemulsion, thermal evaporation, and the redox reaction mechanism [5–8]. There is newly emerging interest in one-dimensional nanostructured SnO₂ materials such as nanobelts, nanotubes, and nanowires, in addition to the extensively studied SnO₂ films and nanoparticles. Recently, attempts have been made to fabricate SnO₂ nanobelts and nanowires for use in sensors for detecting various gases such as carbon monoxide, nitrogen dioxide, and ethanol vapor [9–11]. SnO₂ nanowires have also been researched for application in lithium-ion batteries [12].

Core-shell-structured materials have attracted much attention in physics, chemistry, and material science communities because of their specific structures and unique properties [13, 14]. Advanced materials derived from core-shell composite particles are of extensive scientific and technological interest because of fine-tuning material properties [15]. Wang and his collaborators synthesized a composite of SnO₂ nanoparticles coated on SiO₂ microspheres and found a marked blueshift phenomenon [16]. One-dimensional (1D) heterostructured nanomaterials have attracted great attention due to their novel and distinct properties, and more effort has been taken to explore possible high-performance nanodevices based on them [17, 18]. Synthesis of SnO₂-CuO heterojunction using electrospinning has been reported for application in detecting CO [19]. All inorganic frameworks of tin dioxide shell as cathode material improve cycle performance for lithium-sulfur batteries [20]. Xu et al. improved the mechanical integrity and three-dimensional electron transport for lithium batteries by heterogeneous branched core-shell SnO₂-PANI nanorods [21].

✉ Hong Quan Liu
15192090861@163.com

¹ Department of Materials Science and Engineering, Shandong University of Science and Technology, Qingdao 266510, People's Republic of China

So far, a 1D $\text{SnO}_2\text{-SiO}_x$ core-shell heterostructured nanorod has not been reported in the literature. SnO_2 and SiO_x show high storage capacities as electrode materials [2, 22], but the high storage capacities fade quickly with cycling due to severe volume expansion. Heterostructured materials have been shown in other systems to prevent the electrochemical degradation induced by enormous volume changes during Li^+ insertion or extraction [23]. In this paper, we report a one-step preparation method for SnO_2 nanorods with a coaxially grown SiO_x overlayer and the vertical selective growth is accomplished by adjusting the kinetic parameters. The morphology and growth process of the 1D free-standing core-shell heterostructure are also discussed in detail.

2 Experimental methods

The synthesis system used here includes a high-temperature horizontal tube furnace. A quartz tube with an outer diameter of 50 mm and a length of 1200 mm was placed inside the furnace. Iodine powder 2–6 g in an alumina boat was placed upstream of the growth site in the quartz tube, just outside of the tube furnace. Sn particles were used as the evaporation source. The evaporation materials were placed in an alumina boat and loaded into the center of the tube furnace. At high temperatures $T = 1050\text{ }^\circ\text{C}$, sublimed iodine reacts with Sn to produce a gaseous product of metal iodide that is carried downstream by argon gas flow to a different temperature zone $900\text{--}1000\text{ }^\circ\text{C}$, where it reacts with oxidized Si substrates. Argon (99.9 % pure) was made to flow at atmospheric pressure through the reaction tube at a high rate before synthesis and then reduced to a lower flow rate of 10–60 SCCM during synthesis (SCCM denotes cubic centimeter per minute at standard temperature and pressure).

Oxidized Si substrates were produced from silicon wafer chips roughly etched using a wet oxidation treatment: Si

substrates were heated in a stirred “metal etch” solution (30 % H_2O_2 :37 % HCl : H_2O ; 1:1:5 v/v) at $70\text{ }^\circ\text{C}$ for 20 min, followed by rinsing in deionized water and air-drying.

The morphology of the as-grown products was examined using a field emission scanning electron microscope (SEM, HITACH S-4800). Transmission electron microscopy (TEM) samples were prepared by scripting as-grown substrate using copper grids. The selected area electron diffraction (SAED) patterns and high-resolution transmission electron microscope (HRTEM) images were obtained using a JEOL JEM-2010 microscope.

3 Results and discussion

A typical process for synthesizing coaxial $\text{SnO}_2\text{-SiO}_x$ heterostructured nanorods is described as follows. The center temperature of furnace is fixed at $1050\text{ }^\circ\text{C}$, and oxidized Si substrates are placed downstream where the temperature is about $950\text{ }^\circ\text{C}$. Flow of argon was controlled at a rate of 30 SCCM. The free-standing nanorods and nanotubes shown in Fig. 1 were prepared via the above process. As shown in Fig. 1a, a large number of nanorods randomly grow on the oxidized substrates. As-grown depositions show a uniform morphology characterized by multi-prism shape, smooth surface, a diameter of 100–200 nm, and a length of 1–2 μm , as presented in Fig. 1a, b. The multi-prism morphology is similar to the SnO_2 nanorod morphology of another report [24]. The nanorods grow from the substrates and are not simply deposits on the substrates.

The element line distribution of a single nanorod is shown in Fig. 2. There are composition fluctuations of three elements (Si, Sn, and O) as shown in Fig. 2. Though Fig. 2 shows a reduction in Si content, this apparent reduction is related to a strong Si background from the

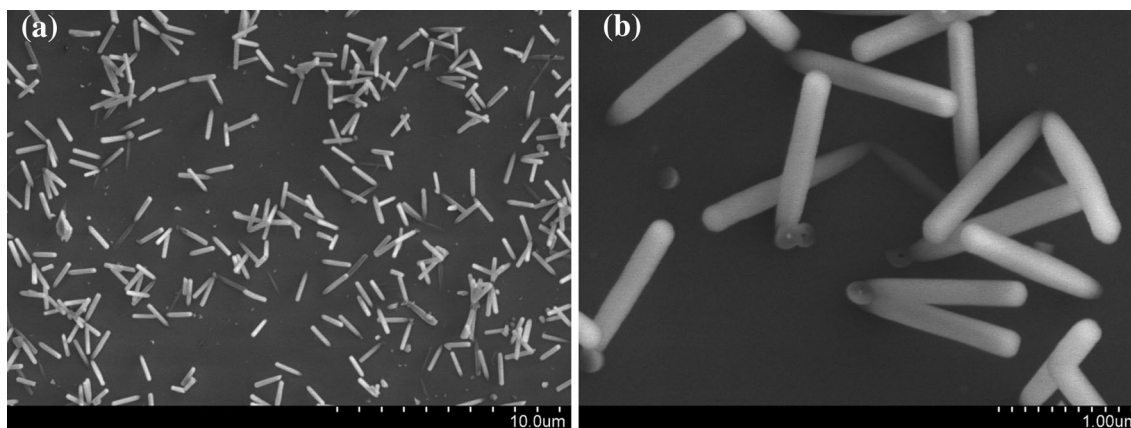


Fig. 1 Morphology of nanorods under typical synthesis process

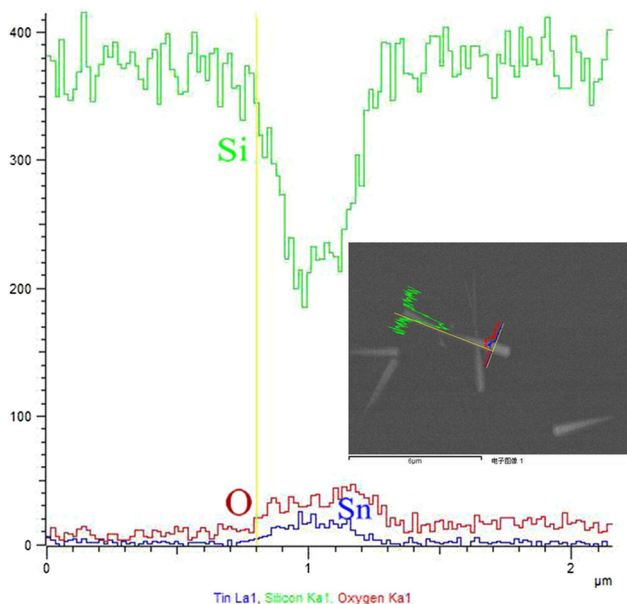


Fig. 2 Element line distribution of nanorods under typical synthesis process

substrate. It can be concluded from these data that the compositions of the nanorods may include Si, Sn, and O.

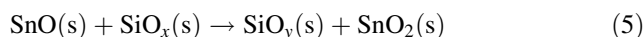
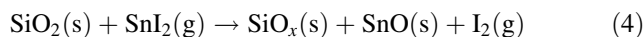
Transmission electron microscopy further confirms that the nanorod appears to have a smooth surface, but is covered with a shell layer. The diameter of the nanorod measured by TEM is similar to the result of above SEM observation. From the selective diffraction pattern in inset of Fig. 3a, it can be seen that a characteristically amorphous halo pattern and a crystalline diffraction pattern occur simultaneously. The crystalline diffraction pattern is difficult to index due to screening from the amorphous layer. To verify core-shell substance phase and composition, selective diffraction patterns and energy spectra should be characterized after removing the amorphous layer. Figure 3b shows the TEM photograph of a nanorod with part of the shell layer removed. An amorphous SiO_x shell layer (area labeled as 1 in Fig. 3b) is verified by energy spectrum shown in Fig. 3c. As shown in Fig. 3d, there is no Si element in energy spectrum of core layer (zone labeled as 2 in Fig. 3b). From these data, it may be concluded that the phase of core layer material should be tin oxide. The chemical composition from energy spectrum corresponds with the element line distribution results from SEM.

In order to analyze phase and microstructure of the core layer, we observe the lattice fringe phase and selective diffraction pattern for 2 zones in Fig. 3b. The core material phase is concluded as SnO₂ by the selective diffraction pattern shown in inset of Fig. 4. Spacing between (101) planes in SnO₂ crystal is corresponding to spacing

(2.65 nm) of lattice fringe phase shown in Fig. 4, so the growth direction of nanorod is the [101].

According to the theoretical calculation of SnO₂ crystal surface energy, the sequence of surface energy per crystal face is (110) < (100) < (101) ≪ (001) [25]. The (110) facet has the lowest surface energy, and [110] should be a reasonable growth direction according to the thermodynamical stability. Theoretical calculation of SnO₂ crystal surface energy originates from the perfect crystal, but there are different defects in different processes. Those defects could affect the value of crystal surface energy. Theoretical calculation and experimental evidence all suggest that the reduced (101) surface has a lower surface energy than the (110) surface [26, 27]. In our process, low oxygen partial pressure and high reaction temperature are advantageous to form the reduced (101) surface. So the [101] growth direction in our process also satisfies the lowest energy principle in thermodynamics.

The process for synthesizing free-standing SnO₂-SiO_x core-shell nanorods includes chemical vapor transport, nucleation, and growth. Probable reactions are shown as follows.



Tin easily evaporates at 1050 °C (as shown in reaction 1), and it can react with iodine vapor upstream (as shown in reaction 2). Then gaseous product (SnI₂) was transported to the growth zone for nucleation and growth under Ar flow. The amorphous SiO_x layer appears on the substrate after wet-etching, and then dismutation reaction (reaction 3) occurs for SiO_x at high temperature [28]. The SiO₂ microzone produced by reaction 3 provides a site of heterogeneous nucleation. At the nucleation site, the reactions about SnI₂ and SiO₂ may occur according to reactions 4 or 5. A core-shell (SnO₂-SiO_x) structure should thus be synthesized due to the phase separation in order to reduce interface energy between the two phases [29]. The extremely precise control of core-shell size and thickness requires a better understanding of the core-shell growth mechanism, and further experiment is underway in our research group.

In order to clarify the kinetic process of synthesizing free-standing nanorods, the synthesis conditions (temperature, gas flow, state of substrate, and I₂ content parameters) are tuned. The reaction and deposition temperature directly affects the chemical reaction and surface adsorption and thus changes the morphology of deposited

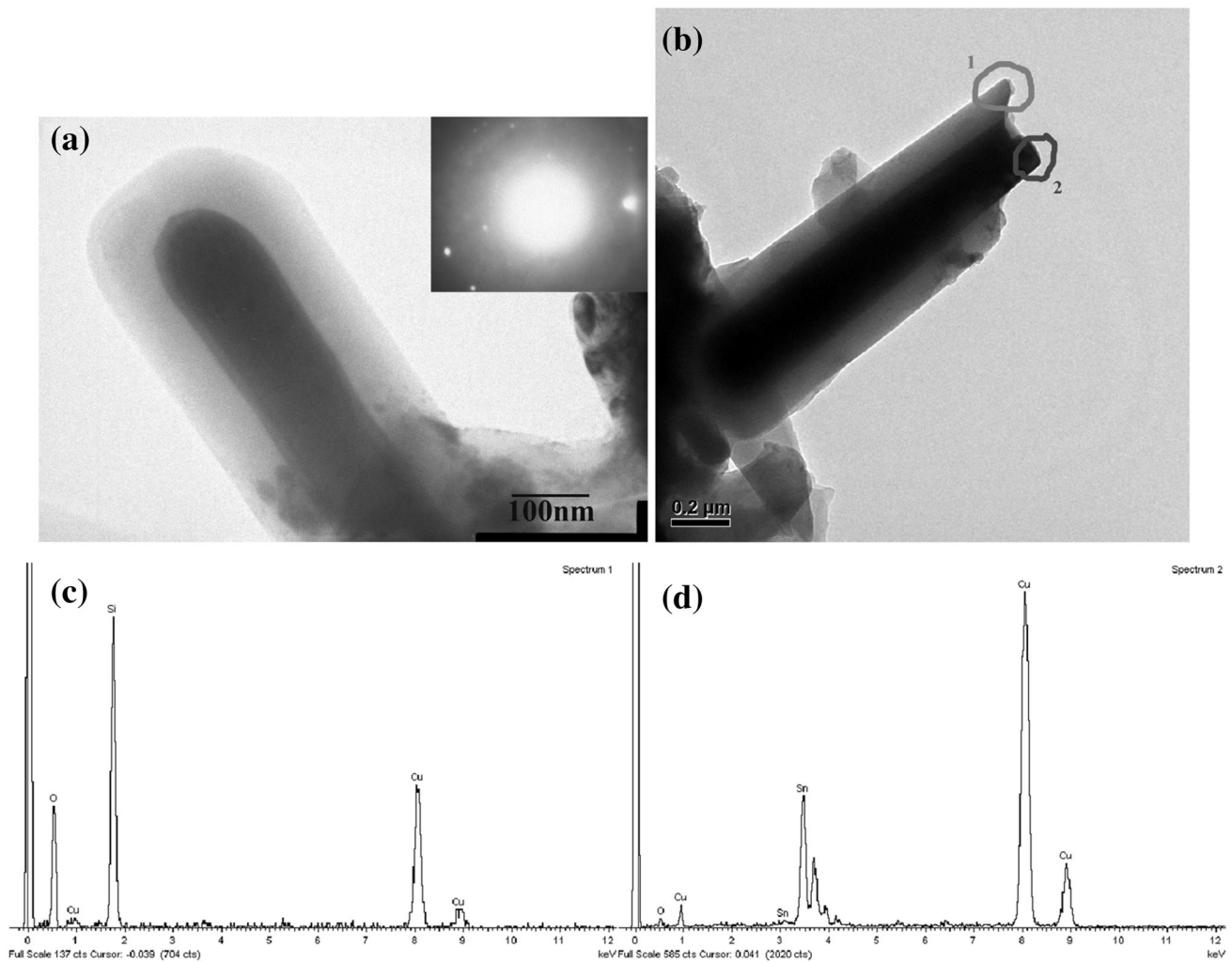


Fig. 3 TEM image and energy spectrum of a nanorod

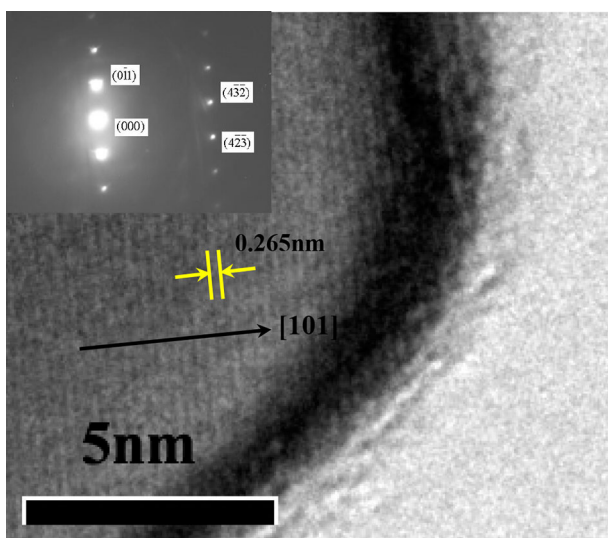


Fig. 4 Lattice fringe phase, selected diffraction of SnO₂ core

materials. Surface adsorption should be performed first before deposition; the adsorption ability can be described as follows.

$$\sigma = \tau F \quad (6)$$

$$\tau = \tau_0 \exp[\Delta H_{\text{ads}}/RT] \quad (7)$$

$$F = 3.5 \times 10^{22} \frac{P}{\sqrt{MT}} \quad (8)$$

where σ , τ , F , τ_0 , ΔH_{ads} , R , T , P , M are the surface coverage, the average residence time, the gas incidence flux, constant relation with vibration period, adsorption heat, gas constant, absolute temperature, vapor pressure of adsorbed molecular, and relative molecular mass.

In the case of other constant parameters, higher (1150 °C) and lower (950 °C) temperatures result in no obvious product deposition. Though higher temperature is beneficial for promoting chemical reactions, it is also an

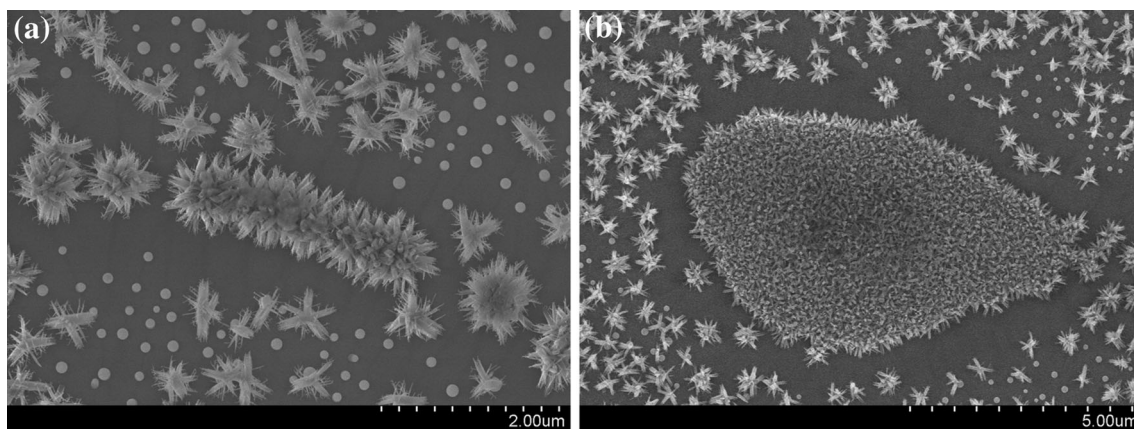


Fig. 5 Deposited materials morphology under gas flow of 60 SCCM

obstacle for surface adsorption. The limited surface adsorption and the limited reaction cases occur at high temperature and low temperature, respectively. Deposition therefore only occurs at the proper temperature.

At proper temperature, the morphology of deposition is also directly controlled by the mass transfer coefficient. In the open chemical vapor deposition system, gas flow near substrates may be considered as fitting the laminar flow model. Diffusion is always the dominant transport mechanism near the surface of a solid substrate. According to the laminar model, the mass transfer coefficient may be described as follows [30].

$$h_{mi} = 0.664 \frac{D}{l} \text{Re}_x^{1/2} \text{Sc}^{1/3} \quad (9)$$

where h_{mi} , l , Re_x , Sc , D are the mass transfer coefficient, characterized length, Reynolds number, Schmidt number, and diffuse coefficient.

After deducing,

$$h_{mi} = 0.664 \left(\frac{v}{l}\right)^{1/2} \left(\frac{\rho}{\eta}\right)^{1/6} D^{2/3} \quad (10)$$

where h_{mi} , v , l , ρ , η , D are the mass transfer coefficient, the velocity of gas flow, characterized length, fluid density, viscosity, and diffuse coefficient.

The mass transfer coefficient may be controlled by adjusting gas flow. When flow was adjusted to a lower value (10 SCCM), there is no obvious disposition on substrates due to an insufficiently large mass transfer coefficient. When gas flow was controlled at 30 SCCM, free-standing nanorods were deposited on substrate (shown in Fig. 1). Adjusting gas flow to the bigger value (60 SCCM), as-grown depositions on substrate appear with shrimp-like, flower-like, and worm-like morphologies (shown in Fig. 5a, b). The vertical growth and horizontal growth models are now presented according to the morphology

difference shown in Figs. 1 and 5. The limited resource was transferred to substrate under a proper gas flow (30 SCCM). The limited resource was selectively adsorbed on the growth nucleus, so free-standing nanorods appear on substrate. This selective grow process is considered as the vertical growth model. Under a greater gas flow, more resource was transferred to substrate due to the larger mass transfer coefficient. The surplus resource accelerates the horizontal growth of nanomaterial. The horizontal growth model is similar to the initial stage of film deposition [31].

State of substrate and content of I₂ also affect nucleation and chemical transport during synthesis, respectively. There is no obvious substance deposition without I₂ or with untreated Si substrate.

4 Conclusions

The free-standing coaxial SnO₂-SiO_x core-shell structure nanorods were synthesized by the CVT method. The coaxial SnO₂-SiO_x heterostructured nanorods appear with uniform morphology, smooth surface, a diameter of 100–200 nm, and a length of 1–2 μm. The low oxygen partial pressure and high reaction temperature in our process make the reduced (101) surface, which has a lower surface energy than the (110) surface. So the [101] growth direction is also reasonable according to the lowest energy principle in thermodynamics. The SiO_x dismutation reaction provided the nucleation site, and formation of core-shell (SnO₂-SiO_x) structure should result from the phase separation energy. The vertical growth and horizontal growth models may be controlled by adjusting the mass transfer coefficient. Free-standing nanorods only appear under the condition favorable to the vertical growth model. Shrimp-like, flower-like, and worm-like morphologies occur under the condition for the horizontal growth model.

Acknowledgments The authors would like to thank the financial supports from the TaiShan Scholars Project of Shandong (TS20110828), Shandong Natural Science Foundation Project (Grant No. ZR2015EM013), and a Project of Shandong Province Higher Educational Science and Technology Program (Grant No. YA07).

References

1. K. Akash, U.A. Zain, W.K. Hyoun et al., *ACS Appl. Mater. Interfaces* **8**(4), 2486 (2016)
2. S.H. Ayorinde, M. Kathleen, R. Ramu et al., *J. Phys. Chem. C* **120**(4), 2036 (2016)
3. Y.Y. Li, H.Y. Zhang, Y.M. Chen et al., *ACS Appl. Mater. Interfaces* **8**(1), 197 (2016)
4. J.J. Ding, X.B. Yan, J. Li et al., *ACS Appl. Mater. Interfaces* **3**(11), 4299 (2011)
5. K. Sato, Y. Yokoyama, J. Valmalette et al., *Cryst. Growth Des.* **13**(4), 1685 (2013)
6. F. Gyger, M. Hübner, C. Feldmann et al., *Chem. Mater.* **22**(16), 4821 (2010)
7. M. Herrera, D. Maestre, A. Cremades et al., *J. Phys. Chem. C* **117**(17), 8997 (2013)
8. J. Zhang, J. Guo, H. Xu et al., *ACS Appl. Mater. Interfaces* **5**(16), 7893 (2013)
9. Y. Wang, X. Jiang, Y. Xia et al., *J. Am. Chem. Soc.* **125**, 16176 (2003)
10. B. Cai, X.L. Zhao, T.F. Pei et al., *Appl. Phys. Lett.* **104**(7), 073112 (2014)
11. M. Li, L.J. Qiao, W.Y. Chu et al., *Sens Actuators B Chem* **158**(1), 340 (2011)
12. Z.L. Yang, S.P. Zhao, W. Jiang et al., *Electrochim. Acta* **158**, 321 (2015)
13. F. Tao, M.E. Grass, Y.W. Zhang et al., *Science* **322**, 932 (2008)
14. K.W. Qiu, Y. Lu, D.Y. Zhan et al., *Nano Energy* **11**, 687 (2015)
15. M. Amato, R. Rurali et al., *Nano Lett* **15**(5), 3425 (2015)
16. X.F. Duan, Y. Huang, R. Agarwal et al., *Nature* **421**, 241 (2003)
17. F. Rossell, A. Bertoni, D. Ercolani et al., *Nat. Nanotechnol.* **9**, 997 (2014)
18. L.Q. Mai, F. Yang, Y.L. Zhao et al., *Nat. Commun.* **2**, 381 (2011)
19. S.L. Bai, W.T. Guo, J.H. Sun et al., *Sens. Actuators B Chem.* **226**, 96 (2016)
20. L.P. Zhang, Y.F. Wang, S.Q. Gou et al., *J. Phys. Chem. C* **119**(52), 28721 (2015)
21. C.C. Ling, Q.Z. Xue, Z.D. Han et al., *Sens. Actuators B Chem.* **227**, 438 (2016)
22. J. Yang, Y. Takeda, N. Imanishi et al., *Solid State Ionics* **152–153**, 125 (2002)
23. Y.M. Kang, M.S. Park, J.Y. Lee et al., *Carbon* **45**, 1928 (2007)
24. W.Z. Wang, C.K. Xu, X.S. Wang et al., *J. Mater. Chem.* **12**, 1922 (2002)
25. E.R. Leite, T.R. Giraldi, F.M. Pontes et al., *Appl. Phys. Lett.* **83**, 1566 (2003)
26. C.H. Xu, Y. Jiang, D.Q. Yi et al., *J. Appl. Phys.* **111**(6), 063504 (2012)
27. G.X. Zhou, X.L. Wu, L.Z. Liu et al., *Appl. Surf. Sci.* **349**(15), 798 (2015)
28. F. Yubero, A. Barranco, J.A. Mejías et al., *Surf. Sci.* **458**, 229 (2000)
29. H. Choi, J.C. Johnson, R. He, *J. Phys. Chem. B* **107**(34), 8721 (2003)
30. F.P. Incropera, D.P. Dewitt, T.L. Bergman, *Fundamentals of Heat and Mass Transfer*, 6th edn. (Wiley, Hoboken, 2007), pp. 410–411
31. P. Jedrzejowski, A. Amassian, E. Bousser et al., *Appl. Phys. Lett.* **88**, 071915 (2006)